

Stable subpicosecond soliton fiber laser passively mode-locked by gigahertz acoustic resonance in photonic crystal fiber core: supplementary materials

M. PANG,^{1,*} X. JIANG,¹ W. HE,¹ G. K. L. WONG,¹ G. ONISHCHUKOV,¹ N. Y. JOLY,¹ G. AHMED,¹ C. R. MENYUK,² AND P. ST.J. RUSSELL¹

¹Max Planck Institute for the Science of Light, Guenther-Scharowsky-Strasse 1, 91058 Erlangen, Germany

²Department of Computer Science and Electrical Engineering, University of Maryland Baltimore County, Baltimore, MD, 21250, USA

*Corresponding author: meng.pang@mpl.mpg.de

Published 30 March 2015

This document provides supplementary information to “Stable subpicosecond soliton fiber laser passively mode-locked by gigahertz acoustic resonance in photonic crystal fiber core,” <http://dx.doi.org/10.1364/optica.2.000339>. We provide a detailed description of the acoustic wave generation in the solid-core silica photonic crystal fiber and some additional system parameters and experimental results. © 2015 Optical Society of America

<http://dx.doi.org/10.1364/optica.2.000339.s001>

1. Acoustic wave generation

We begin with the acoustic wave equation driven by an electrostrictive effect [S1]:

$$\frac{\partial^2 \rho}{\partial t^2} - v_a^2 \left(1 + \Gamma \frac{\partial}{\partial t} \right) \nabla^2 \rho = \nabla \cdot \mathbf{f} \quad (\text{S1})$$

where ρ is the material density variation from its mean value of ρ_0 , v_a is the sound velocity, Γ is the damping factor of the acoustic wave and \mathbf{f} is the driving stress created through electrostriction [S1]:

$$\mathbf{f} = -\frac{1}{2} \varepsilon_0 \gamma_e \nabla E^2 \quad (\text{S2})$$

where ε_0 is the electric permittivity in vacuum, γ_e is the electrostrictive constant of fused silica, and E is the electric field of the linearly polarized light propagating in the PCF.

The driving optical pulse train has repetition rate Ω and individual pulse energies of E_p . The fundamental optical mode in the PCF has the largest overlap integral with the first-order radial (R_{01}) acoustic mode [S2], and in practice the repetition rate of the pulsed light is close to the resonance frequency of this acoustic mode, while the resonance linewidth is quite narrow (mechanical quality factor ~ 250 [S2]). If we consider only the fundamental frequency component of the optical pulse train and neglect optical loss (< 0.05 dB/m) in the PCF, the electrostrictive term driving the R_{01} acoustic mode is given by [S2]:

$$\nabla \cdot \mathbf{f} = -\frac{1}{4} \varepsilon_0 \gamma_e s_1 \nabla_{\perp}^2 E_0^2 e^{i(\Omega t - qz)} + \text{c.c.} \quad (\text{S3})$$

where E_0 is the normalized field distribution of the optical mode in the PCF core, q its propagation constant, ∇_{\perp}^2 the transverse Laplacian operator, and s_1 is given by:

$$s_1 \approx \frac{1}{T_p} \int_{-T_p/2}^{T_p/2} A^2(z, t) dt = \frac{E_p \Omega}{\pi n_{\text{eff}} \varepsilon_0 c A_{\text{eff}}} \quad (\text{S4})$$

where $A(z, t)$ is the slowly varying pulse envelope, $T_p = 2\pi/\Omega$ is time between pulses, n_{eff} the effective refractive index, A_{eff} the effective mode area of the optical mode and c is the speed of light in vacuum. In Eq. (S4) the duration of the optical pulse is assumed to be much shorter than the period of the excited acoustic wave.

The acoustic modes supported by the PCF core are given by the modal equation [S3] as:

$$\nabla_{\perp}^2 \rho_{mn}(r, \theta) + \left(\frac{\Omega_{mn}^2}{v_a^2} - q^2 \right) \rho_{mn}(r, \theta) = 0 \quad (\text{S5})$$

where $\rho_{mn}(r, \theta)$ is the normalized mode profile of different acoustic modes and Ω_{mn} is the eigenfrequency of the (m, n) -th acoustic mode. Using finite element modelling and setting q equal to zero, we can simulate the density variation distribution of acoustic modes supported by the PCF structure (scanning electron micrograph of the PCF is shown in Fig. 1). The simulations predict

that the R_{01} acoustic mode has a resonant frequency $\Omega_{01} = 2.05$ GHz, which is reasonably close to the measured value of 2.13 GHz [S2]. Its acoustic mode profile is shown in Fig. S1a, the fundamental optical mode profile in silica being shown in Fig. S1b for comparison. We also numerically calculated the magnitude of the overlap integral between the fundamental optical mode and the R_{01} acoustic mode to be $2.4 \mu\text{m}^{-2}$.

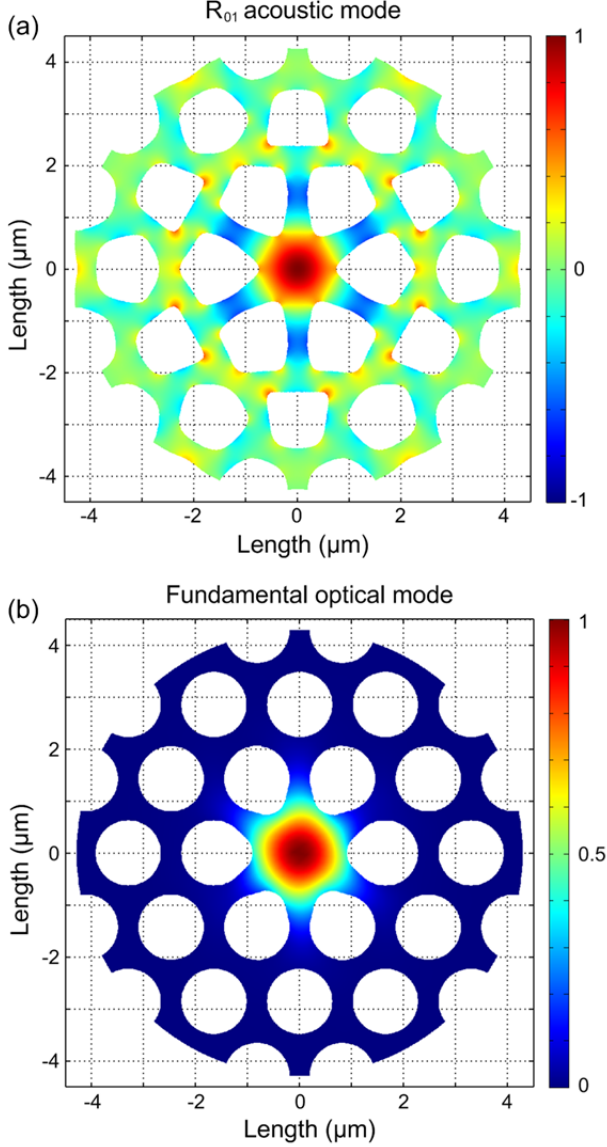


Fig. S1. (a) Simulated normalized density variation (color map) and material deformation of the R_{01} acoustic mode in the PCF profile. (b) Normalized electric field distribution (color map) of the fundamental optical mode in the silica PCF.

By inserting Eq. (S3), Eq. (S4) and Eq. (S5) into Eq. (S1), we obtain the steady-state equation as:

$$\begin{aligned} -ib\rho_{01}(r,\theta)\Omega\Gamma_B - b\rho_{01}(r,\theta)(\Omega^2 - \Omega_{01}^2) \\ = -\frac{1}{2}\epsilon_0\gamma_e\nabla_{\perp}^2 E_0^2 \cdot s_1 \end{aligned} \quad (\text{S6})$$

where b is the amplitude, $\rho_{01}(r,\theta)$ is the normalized mode profile, and $\Gamma_B = \Omega_{01}^2\Gamma$ is the Brillouin linewidth of the R_{01} acoustic mode. Finally by multiplying both sides of Eq. (S6) by $\rho_{01}(r,\theta)$ and integrating over the transverse plane, we obtain:

$$b = \frac{-\epsilon_0\gamma_e s_{01} \langle \rho_{01}(r,\theta) \nabla_{\perp}^2 E_0^2 \rangle}{2(\Omega_{01}^2 - \Omega^2 - i\Omega\Gamma_B) \langle \rho_{01}^2(r,\theta) \rangle} \quad (\text{S7})$$

where we denote integrated quantities by angle brackets as $\langle f(r) \rangle = \int_0^{2\pi} \int_0^{\infty} f(r,\theta) r dr d\theta$, and $Q = \langle \rho_{01}(r,\theta) \nabla_{\perp}^2 E_0^2 \rangle / \langle \rho_{01}^2(r,\theta) \rangle$ is the overlap integral of the R_{01} acoustic mode with the electrostrictive stress field. Thus the acoustic wave generated by the driving optical pulses may be written as:

$$\rho(z,t,r,\theta) = \frac{\gamma_e |Q| E_p \rho_{01}(r,\theta) e^{i(\Omega t - qz)}}{4\pi n_{\text{eff}} c A_{\text{eff}} [2(\Omega_{01} - \Omega) - i\Gamma_B]} + \text{c.c.} \quad (\text{S8})$$

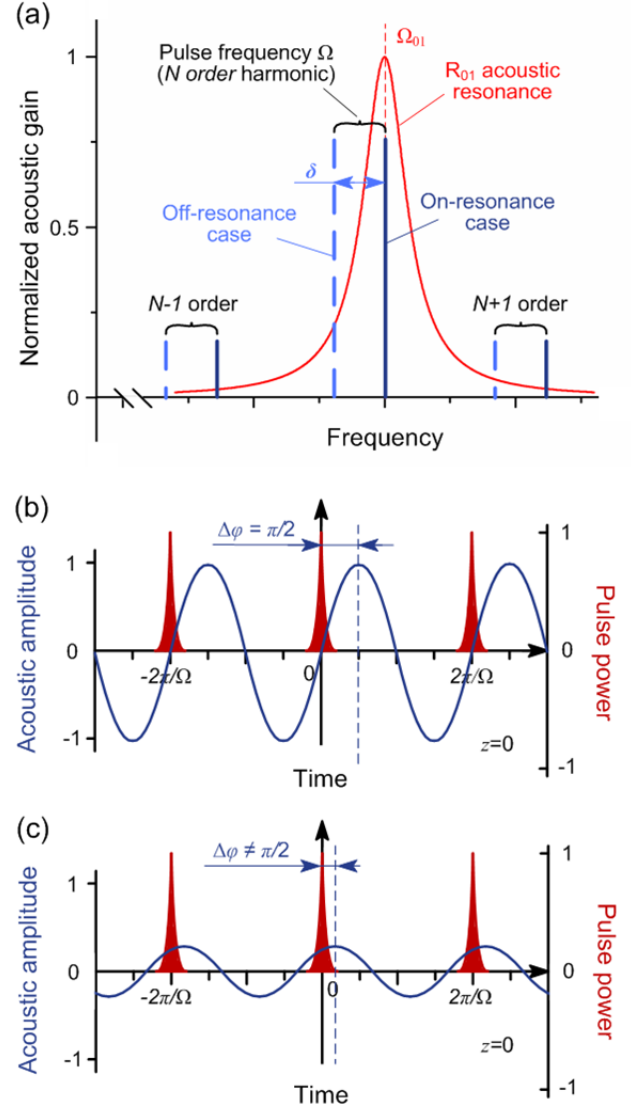


Fig. S2. (a) Gain spectrum of an acoustic mode with resonant frequency Ω_{01} . Repetition rate of the driving pulse train is at the N^{th} order harmonic of the cavity round-trip frequency. Full blue line: on-resonance case $\Omega = \Omega_{01}$. Light-blue dashed line: off-resonance case $\Omega \neq \Omega_{01}$. (b) The $\pi/2$ relative phase shift between the acoustic wave and its driving pulse train in the on-resonance case. (c) Illustrating the decrease in acoustic amplitude, and shift in acoustic phase, when the repetition rate of the driving pulse train is detuned from the acoustic resonant frequency.

In the experiments, the repetition rate Ω of the optical pulses is equal to an integer multiple of the round-trip frequency (N^{th} order harmonic as shown in Fig. S2a), while the resonant frequency Ω_{01}

of the R_{01} acoustic mode is given by the PCF structure. We denote the frequency difference between them as $\delta = \Omega - \Omega_{01}$, and by using Eq. (S8) the acoustic wave can be expressed as:

$$\rho(z, t, r, \theta) = \frac{\gamma_e |Q| E_p \rho_{01}(r, \theta) e^{i(\Omega t - qz - \Delta\varphi)}}{4\pi n_{\text{eff}} c A_{\text{eff}} \sqrt{4\delta^2 + (\Gamma_B)^2}} + \text{c.c.} \quad (\text{S9})$$

where $\Delta\varphi$ is the relative phase offset between the acoustic wave and its driving pulse train given by:

$$\Delta\varphi = \text{arccot}(-2\delta / \Gamma_B), \quad 0 \leq \Delta\varphi \leq \pi \quad (\text{S10})$$

From Eq. (S9), we see that the amplitude of the generated acoustic wave is inversely proportional to $(4\delta^2 + \Gamma_B^2)^{1/2}$. Acoustic gain appears when the phase shift $\Delta\varphi$ between the driving pulse train and the acoustic wave (Eq. (S10)) lies within the range of $(0, \pi)$ [S1,S2]. In a manner similar to a driven oscillator with a single degree of freedom [S4], the amplitude of the acoustic wave reaches its maximum value in the on-resonance case ($\delta = 0$) as illustrated in Fig. S2b, where $\Delta\varphi = \pi/2$. In the off-resonance case $\Delta\varphi \neq \pi/2$ (Fig. S2c) and the amplitude of the acoustic wave decreases.

Using Eq. (S8) we can obtain the modulation of material relative permittivity $\Delta\epsilon_r(z, t, r, \theta)$ due to the optoacoustic effect:

$$\begin{aligned} \Delta\epsilon_r(z, t, r, \theta) &= \gamma_e \frac{\rho}{\rho_0} \\ &= \frac{\gamma_e^2 |Q| E_p \rho_{01}(r, \theta) e^{i(\Omega t - qz - \Delta\varphi)}}{4\pi n_{\text{eff}} c A_{\text{eff}} \rho_0 \sqrt{4\delta^2 + (\Gamma_B)^2}} + \text{c.c.} \end{aligned} \quad (\text{S11})$$

Using Eq. (S10) and Eq. (S11) we can roughly estimate the amplitude of the index modulation generated by the optical pulses in the center of the PCF core. When the PCF has a core diameter of $1.8 \mu\text{m}$ corresponding to an effective mode area of $2.54 \mu\text{m}^2$ and the pulse energy is 25 pJ , by using $\gamma_e = 1.17$, $|Q| = 2.4 \mu\text{m}^{-2}$, $n_{\text{eff}} = 1.46$, $c = 3 \times 10^8 \text{ m/s}$, $\rho_0 = 2.2 \times 10^3 \text{ kg/m}^3$, $\delta = 2\pi \times 5 \text{ MHz}$ and $\Gamma_B = 2\pi \times 8.1 \text{ MHz}$, we obtain that $\Delta\varphi = 0.22\pi$ with a generated refractive index modulation of $\sim 2 \times 10^{-8}$, which is around two orders of magnitude larger than the optoacoustic-induced index modulation in conventional step-index fiber [S5,S6].

2. Kerr nonlinearity and dispersion maps in the laser cavity

The 0.6 m length of PCF has Kerr nonlinearity $36.3 \text{ km}^{-1}\text{W}^{-1}$ and dispersion $-119 \text{ ps}^2/\text{km}$ at 1560 nm . The 0.2 m length of highly nonlinear fiber (HNLF) has Kerr nonlinearity $10.3 \text{ km}^{-1}\text{W}^{-1}$ and dispersion $19.8 \text{ ps}^2/\text{km}$, and the 0.6 m erbium-doped fiber a Kerr nonlinearity of $9.3 \text{ km}^{-1}\text{W}^{-1}$ and a dispersion of $77 \text{ ps}^2/\text{km}$. The remaining fiber in the cavity is conventional SMF28 with length of 10.8 m , a Kerr nonlinearity of $1.1 \text{ km}^{-1}\text{W}^{-1}$ and a dispersion of $-22.8 \text{ ps}^2/\text{km}$. We calculated a cavity-average Kerr nonlinearity coefficient of $3.4 \text{ km}^{-1}\text{W}^{-1}$ and a group-velocity dispersion of $-21.9 \text{ ps}^2/\text{km}$. Then, based on the fundamental soliton assumption [S7], the product of pulse energy and FWHM duration would be $22.7 \text{ pJ}\cdot\text{ps}$, which is quite close to the value of $14.1 \text{ pJ}\cdot\text{ps}$ estimated from the experimental results.

The Kerr nonlinearity dominates the pulse shape (leading to soliton formation in the steady state), whereas the much slower optoacoustic nonlinearity locks the pulse repetition rate. While the fast saturable absorber (based on nonlinear polarization rotation) does not really contribute to pulse shaping, it plays an important role in helping the laser self-start as well as stabilizing the mode-locking by suppressing the background radiation.

3. Amplitude noise and timing jitter

To estimate the short-term pulse amplitude noise, the laser baseband single-sideband (SSB) noise spectrum was measured as a function of off-set frequency from 0 Hz . The results are shown in Fig. S3a, with the noise floor of the 26 GHz electrical spectrum analyzer (ESA) and 30 GHz photodetector as a reference. In this baseband noise spectrum, sharp peaks at $\sim 1 \text{ kHz}$ correspond to acoustic/vibrational perturbations. By integrating this baseband noise, we estimate the relative amplitude noise to be $\sim 0.1\%$ over a bandwidth from 1 Hz to 1 MHz [S8,S9].

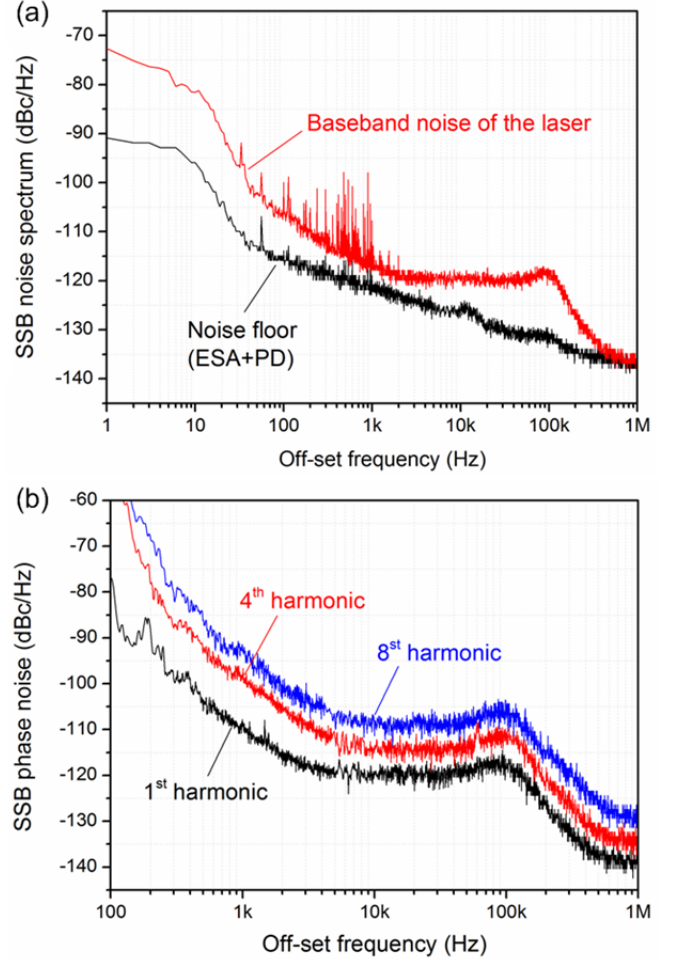


Fig. S3. (a) Measured baseband SSB noise spectrum of the laser (red curve), and noise floor of the ESA and photodetector (black curve). (b) Measured SSB phase noise spectra for 1st, 4th and 8th harmonics of the pulse repetition frequency.

We also estimated the pulse timing jitter by measuring the SSB noise spectra for different harmonics of the pulse repetition rate. The spectra of the 1st, 4th and 8th harmonics, measured over a frequency range from 100 Hz to 1 MHz , are shown in Fig. S3b. It can be clearly seen that the noise increases strongly for higher harmonic orders, giving direct evidence of temporal jitter in the pulse train [S8]. In this free-running laser without cavity length stabilization, phase noise at low frequencies ($< 10 \text{ kHz}$) is dominated by cavity length perturbations, thus the low-frequency pulse timing jitter should be similar to that of a typical free-running laser mode-locked at the cavity round-trip frequency. Gordon-Haus jitter may be the main noise source at high frequencies. Strong phase modulation through enhanced optoacoustic interactions in the PCF may re-time the pulses and suppress high-frequency timing jitter, just as in lasers that are actively mode-locked with an external phase modulator [S10].

We estimate the relative pulse timing jitter using the expression $\Delta T/T = (2P_{\text{noise}})^{1/2}/(2\pi)$ [S9,S10], where T is the time between pulses, ΔT is the timing jitter and P_{noise} is the SSB noise power integrated over the selected frequency range. The value is ~ 40 fs from 100 Hz to 1 MHz and ~ 26 fs from 10 kHz to 1 MHz. Since the accuracy of these noise measurements using an ESA is limited by the intrinsic amplitude and phase noise of the ESA and the photodetector [S11], the estimated values give only upper limits for the laser amplitude noise and pulse timing jitter.

The pulse energy fluctuations and timing jitter at the fundamental cavity round-trip frequency (i.e., the super-mode noise of the harmonically mode-locked laser [S12]) are at low levels, with a super-mode suppression ratio >50 dB. In the experiment, we observed super-mode noise peaks with small amplitudes and narrow linewidths, off-set from the main comb-lines by multiples of the cavity round-trip frequency f_{RT} . Those super-mode peaks are due to correlated high-frequency noise in the pulse envelope [S10,S12].

4. Optical comb structure

We also measured the optical comb structure by heterodyning with a local oscillator signal from a fiber laser with 2 kHz linewidth at 1550 nm. A tunable optical filter (~ 12 nm bandwidth) was inserted into the cavity and used to tune the central wavelength of the laser close to that of the local oscillator. This filter increased the overall cavity length, reducing the mode-spacing from 16.8 to 13.1 MHz but otherwise having no effect on the lasing characteristics. The beat signal between the mode-locked laser and the local oscillator was measured using a photodetector and the ESA, and the results are shown in Fig. S4. Similar to the case of active high-harmonic mode-locking with a phase modulator [S10,S13], the optical comb structure shows cavity modes with 13.1 MHz spacing (note that frequencies above and below the local oscillator frequency cannot be distinguished in this measurement, resulting in two interleaved frequency combs). We believe that the sub-peaks offset by ~ 1 MHz from the comb lines are artefacts of the local oscillator. The amplitude fluctuations among different comb lines are mainly induced by wavelength drift in both lasers, which shifts the line positions within the measurement time. Decreasing the sweep time of the ESA by using a narrower span and lower resolution can significantly decrease the amplitude fluctuations, however, this would mean that the comb structure could not be so well resolved. As shown in Fig. S4b, the linewidth of an individual comb line is less than 20 kHz (the resolution limit of the ESA).

When the system is stably mode-locked, each soliton circulating in the laser cavity must restore itself (both in phase and in amplitude) after each cavity round-trip, which yields narrow linewidths for the optical comb lines. Preliminary measurements of the heterodyne signal using a fast oscilloscope show that although individual solitons within one cavity round-trip time have arbitrary relative phases, this phase relationship repeats periodically after every round-trip. This is similar to what happens in conventional active mode-locking using a phase modulator [S10,S13].

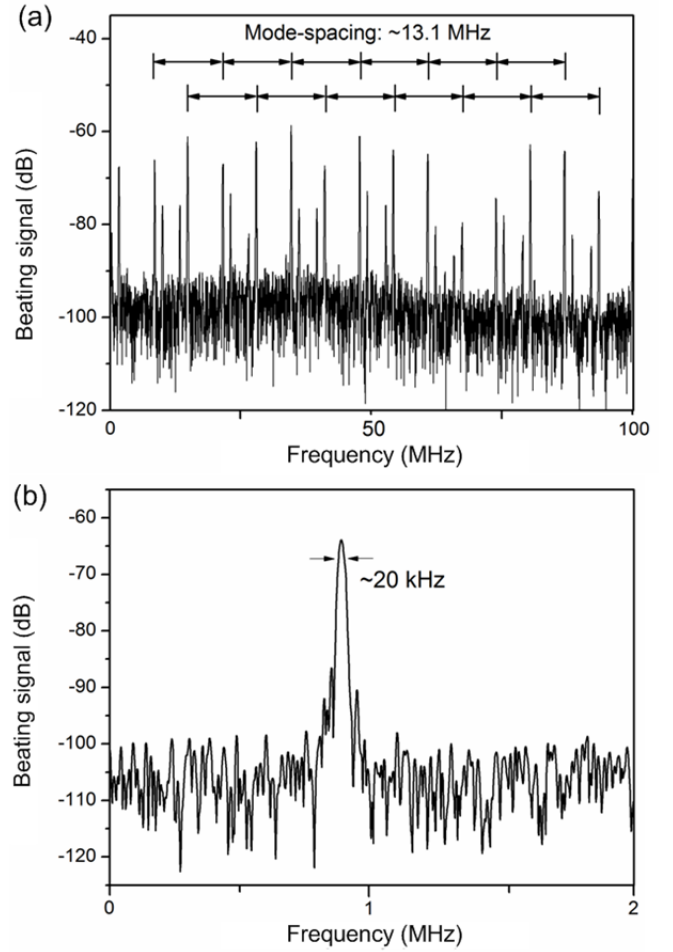


Fig. S4. (a) Heterodyne signal measured by the ESA with 100 kHz resolution bandwidth and (b) a single comb line measured with 20 kHz resolution.

References

- S1. R. W. Boyd, *Nonlinear Optics* (Academic Press, 2008).
- S2. M. S. Kang, A. Nazarkin, A. Brenn and P. St.J. Russell, *Nat. Phys.* **5**, 276 (2009).
- S3. A. Kobaykov, M. Sauer, and D. Chowdbury, *Advance in Opt. and Photon.* **2**, 1 (2004).
- S4. B. H. Tongue, *Principles of Vibration* (Oxford University Press, 2002).
- S5. A. B. Grudinin and S. Gray, *J. Opt. Soc. Am. B* **14**, 144 (1997).
- S6. J. K. Jang, M. Erkintalo, S. G. Murdoch, and S. Coen, *Nat. Photon.* **7**, 657 (2013).
- S7. G. P. Agrawal, *Nonlinear Fiber Optics* (Academic Press, 2007).
- S8. D. von der Linde, *Appl. Phys. B*, **39**, 201 (1986).
- S9. H. A. Haus and A. Mecozzi, *J. Quantum Electron.* **29**, 983 (1993).
- S10. M. E. Grein, A. Haus, Y. Chen and E. P. Ippen, *J. Quantum Electron.* **40**, 1458 (2004).
- S11. J. Kim, J. Chen, J. Cox and F. Kartner, *Opt. Lett.* **32**, 3519 (2007).
- S12. F. Rana, H. L. T. Lee, R. J. Ram, M. E. Grein, L. A. Jiang, E. P. Ippen and H. A. Haus, *J. Opt. Soc. Am. B*, **19**, 2609 (2002).
- S13. M. E. Grein, L. A. Jiang, H. A. Haus and E. P. Ippen, *Opt. Lett.* **27**, 957 (2002).